From antiferromagnetic and hidden order to Pauli paramagnetism in UM_2Si_2 compounds with 5*f* electron duality

Andrea Amorese[a,b], Martin Sundermann[a,b], Brett Leedahl[b], Andrea Marino[b], Daisuke Takegami[b], Hlynur Gretarsson[b,c], Andrei Gloskovskii[c], Christoph Schlueter[c], Maurits W. Haverkort[d], Yingkai Huang[e], Maria Szlawska[f], Dariusz Kaczorowski[f], Sheng Ran[g,1], M. Brian Maple[g], Eric D. Bauer[h], Andreas Leithe-Jasper[b], Philipp Hansmann[b,i], Peter Thalmeier[b], Liu Hao Tjeng[b], and Andrea Severing[a,b,2]

[a]Institute of Physics II, University of Cologne, 50937 Cologne, Germany; [b]Max Planck Institute for Chemical Physics of Solids, 01187 Dresden, Germany; [c]Positron-Elektron-Tandem-Ring-Anlage III (PETRA III), Deutsches Elektronen-Synchrotron, 22607 Hamburg, Germany; [d]Institute for Theoretical Physics, Heidelberg University, 69120 Heidelberg, Germany; [e]van der Waals-Zeeman Institute, University of Amsterdam, 1098 XH Amsterdam, The Netherlands; [f]Institute of Low Temperature & Structure Research, Polish Academy of Science, 50–950 Wroclaw, Poland; [g]Department of Physics, University of California San Diego, La Jolla, CA 92093; [h]MPA-Q, Los Alamos National Laboratory, Los Alamos, NM 87545; and [i]Department of Physics, University of Erlangen-Nuremberg, 91058 Erlangen, Germany

Edited by Gabriel Kotliar, Rutgers, The State University of New Jersey, Piscataway, NJ, and approved October 15, 2020 (received for review March 31, 2020)

Using inelastic X-ray scattering beyond the dipole limit and hard X-ray photoelectron spectroscopy we establish the dual nature of the U 5*f* electrons in UM_2Si_2 (*M* = Pd, Ni, Ru, Fe), regardless of their degree of delocalization. We have observed that the compounds have in common a local atomic-like state that is well described by the U $5f^2$ configuration with the $\Gamma_1^{(1)}$ and Γ_2 quasi-doublet symmetry. The amount of the U $5f^3$ configuration, however, varies considerably across the UM_2Si_2 series, indicating an increase of U 5*f* itineracy in going from *M* = Pd to Ni to Ru and to the Fe compound. The identified electronic states explain the formation of the very large ordered magnetic moments in UPd_2Si_2 and UNi_2Si_2, the availability of orbital degrees of freedom needed for the hidden order in URu_2Si_2 to occur, as well as the appearance of Pauli paramagnetism in UFe_2Si_2. A unified and systematic picture of the UM_2Si_2 compounds may now be drawn, thereby providing suggestions for additional experiments to induce hidden order and/or superconductivity in U compounds with the tetragonal body-centered $ThCr_2Si_2$ structure.

strongly correlated electron systems | X-ray spectroscopy | uranium heavy fermions | hidden order

In heavy fermion compounds the intricate interplay between the f and conduction electrons has a large impact on ground-state properties (1–7). Herein we study uranium $5f$ systems with the UM_2Si_2 composition that crystallize in the tetragonal body-centered $ThCr_2Si_2$ structure whereby M denotes a transition metal. Members of this family exhibit a strong a-c-axis magnetic anisotropy and several of them show long-range magnetic order (e.g., M = Pd, Ni) or remain Pauli paramagnetic (e.g., M = Fe) down to low temperatures (8–16). URu_2Si_2 is special; it undergoes two transitions, one into an ordered state at 17.5 K with a considerable loss of entropy ($\approx 0.2\ R\ln 2$) and a second one at 1.5 K into a superconducting phase (17–19). Below 17.5 K, ordered magnetic moments of 0.03 μ_B have been measured (20, 21), but the moment is too small to account for the loss of entropy. Therefore, it is believed that the phase below 17.5 K is an electronically ordered state but with an order parameter that is yet unknown and continues to be heavily debated to this day; see refs. 22–27 and references therein. This is the famous hidden-order (HO) phase. The application of pressure, however, suppresses the HO phase and a large-moment antiferromagnetic (LMAFM) phase develops. At about 5 kbar the ordered magnetic moment rises discontinuously from 0.03 to about 0.4 μ_B (21, 28). Also, the magnetic field acts to suppress the HO state and instead a spin density wave has been observed (29).

In these uranium systems, the $5f$ electrons are crucial for the ground-state formation. This situation raises the question of whether a systematic picture can be developed that takes into account both correlation effects and band formation with the $5f$ states and at the same time explains consistently the widely varying properties of the UM_2Si_2 compounds. One of the most pressing issues is whether local or atomic-like states can survive the band formation in such metallic systems or, in other words, whether it is meaningful at all to develop models that have atomic multiplet states as a starting point. Otherwise one may be better off using band theory-based methods (refs. 22, 23, 25, 27 and references therein). Very recently nonresonant inelastic X-ray scattering (NIXS) (or X-ray Raman scattering) beyond the dipole limit revealed that local atomic multiplet states can

Significance

The interplay of band-formation and electron-correlation effects in uranium heavy fermion compounds is the subject of an ongoing debate. Here unexpected insight has been gained from advanced spectroscopies on isostructural members of the UM_2Si_2 family with different properties. The antiferromagnetic (*M* = Pd,Ni), hidden order (*M* = Ru), and Pauli-paramagnetic (*M* = Fe) compounds all exhibit atomic-like U $5f^2$ multiplet states with singlet–singlet (quasi-doublet) symmetry while the U $5f^3$ weight increases from Pd→Ni→Ru→Fe, indicating increasing itineracy. This reveals the dual nature of the U-5*f* electrons throughout the family; the local aspects persist in the hidden-order compound URu_2Si_2 and surprisingly even in the highly itinerant Pauli paramagnet UFe_2Si_2. This study gives guidelines for the theoretical treatment of U intermetallic systems.

Author contributions: L.H.T. and A.S. designed research; A.A., M. Sundermann, B.L., A.M., D.T., H.G., A.G., C.S., P.H., L.H.T., and A.S. performed research; Y.H., M. Szlawska, D.K., S.R., M.B.M., E.D.B., and A.L.-J. contributed new reagents; M.W.H. provided the analytic tools; A.A. and M. Sundermann analyzed data; and A.A., M. Sundermann, P.T., L.H.T., and A.S. wrote the paper.

The authors declare no competing interest.

This article is a PNAS Direct Submission.

[1]Present address: Physics Department, Washington University in St. Louis, St. Louis, MO 63130.

[2]To whom correspondence may be addressed. Email: severing@ph2.uni-koeln.de.

This article contains supporting information online at https://www.pnas.org/lookup/suppl/doi:10.1073/pnas.2005701117/-/DCSupplemental.

First published November 17, 2020.

be identified in URu_2Si_2 (30), which is quite surprising since itineracy and Fermi surface effects do play a role in the HO transition (31, 32). It is now important to investigate whether the other members of the UM_2Si_2 family show multiplets and, if so, whether the atomic multiplet states are the same or different across the isostructural family.

For our present study, we selected M = Pd, Ni, Ru, Fe, with Fe (Pd) being isoelectronic with Ru (Ni). The UPd_2Si_2 and UNi_2Si_2 order antiferromagnetically (AF) at T_N = 136 and 124 K, respectively (14, 16), with very large ordered moments; 3.37 (8) and 2.3 μ_B (13) have been reported for UPd_2Si_2 and 2.7 μ_B for UNi_2Si_2 (11). The ordered magnetic moments are, like in URu_2Si_2 under pressure, aligned along the c direction with propagation vectors Q = (0,0,2π/c) at the ordering transition. URu_2Si_2 is the HO compound exhibiting superconductivity, and UFe_2Si_2 is a Pauli paramagnet (PP) down to the lowest temperatures (10, 12, 15). We thus cover a wide range of physical properties while keeping the same U-Si framework and crystal structure ($I4/mmm$). We apply NIXS at the U $O_{4,5}$ edges ($5d \rightarrow 5f$) to determine the presence and symmetry of possible localized $5f$ states. For measuring the degree of delocalization, we utilize U $4f$ core-level photoelectron spectroscopy (PES). This is one of the most powerful spectroscopic methods to study hybridization effects in U compounds (33, 34). Here we apply the hard X-ray version of PES (HAXPES) to make use of the larger probing depth and thus to ensure that the signal is representative for the bulk material.

Our objective is to establish whether the so-called dual nature of the f-electrons model proposed for the description of both the antiferromagnetic order and heavy fermion properties of UPt_3 (35, 36) and UPd_2Al_3 (37, 38) is also a feasible concept to capture the low-energy electronic structure of the hidden order and Pauli paramagnetic members of the UM_2Si_2 family and not only of antiferromagnetic members such as UPt_2Si_2 (39). If so, we may be able to draw a systematic picture which in turn can be used to provide a solid basis for the realistic modeling of the HO transition and to point out further experiments to induce HO or superconductivity in other members of the UM_2Si_2 family.

Results

Ground-State Symmetry with NIXS. In NIXS the directional dependence of the double-differential cross-section gives insight into the orbital anisotropy of the ground state, similar to the linear dichroism in X-ray absorption (XAS). Here the direction of the momentum transfer $\vec{q}$ acts similarly to the direction of the electric-field vector in XAS. The size of the momentum transfer $|\vec{q}|$ makes the important difference; for large momentum transfers NIXS is governed by multipole selection rules while XAS is governed by dipole selection rules. The multipole scattering of the U $O_{4,5}$ edge is more excitonic so that a local atomic approach can be used for a quantitative analysis of the spectra (40). This and further explanations of why the NIXS U $O_{4,5}$ is sensitive to the symmetry of the U configuration that is lowest in energy can be found in ref. 30 and references therein. Further credibility of the U $O_{4,5}$ NIXS method is given in ref. 41, which shows that NIXS confirms the ground-state symmetry of UO_2 that was determined with inelastic neutron scattering.

The dominant NIXS signal arises from Compton scattering and the core-level excitations appear as spikes on top (*SI Appendix*, Fig. S1). Not all core levels have a sizable cross-section at $|\vec{q}|$ = 9.6 Å^{-1}, but the U $O_{4,5}$ core level at 100 eV energy transfer is distinctly visible in all of the spectra. The broad Compton background was used for normalizing the spectra of different $\vec{q}$ directions of one compound. In the second step the data of the U $O_{4,5}$ edges of the different compounds were normalized to each other using the isotropic spectra that are constructed

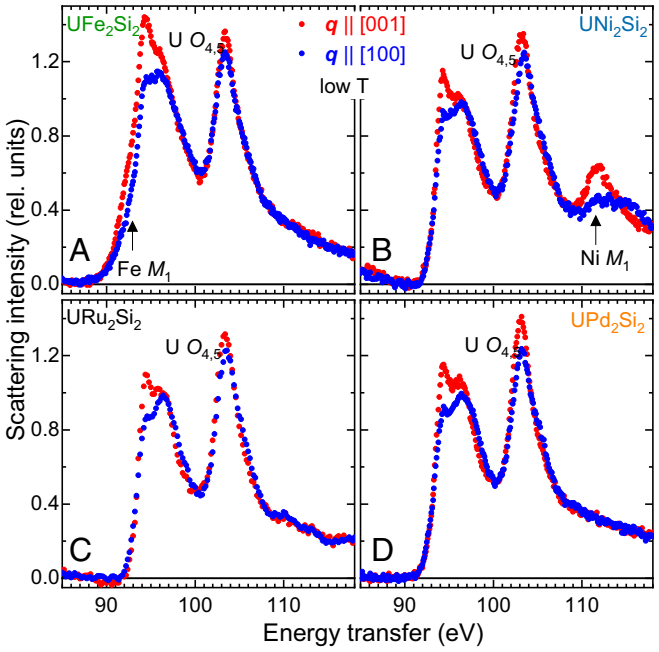

Fig. 1. (*A–D*) Normalized and background-corrected experimental NIXS data $I_{\vec{q}\|[100]}$ (blue dots) and $I_{\vec{q}\|[001]}$ (red dots) at the U $O_{4,5}$ edges ($5d \rightarrow 5f$) at $T < 15$ K. The URu_2Si_2 data in *C* are adapted from ref. 30. The size of the data points represents the statistical error.

from directional-dependent $O_{4,5}$ edge data in Fig. 1 as $I_{iso} = (2 \cdot I_{\vec{q}\|[100]} + I_{\vec{q}\|[001]})/3$.*

Fig. 1 shows the $O_{4,5}$ edge data for T <15 K of UFe_2Si_2 (Fig. 1*A*), UNi_2Si_2 (Fig. 1*B*), URu_2Si_2 (Fig. 1*C*), and UPd_2Si_2 (Fig. 1*D*) for $\vec{q}\|$ [100] (blue) and $\vec{q}\|$ [001] (red) measured with energy steps of 0.1 eV (0.2 eV for M = Ru). The size of the data points reflects the statistical error bars. The data were normalized (see above) and a linear background was subtracted. Finally, the URu_2Si_2 data were reproduced from ref. 30.

All four spectra in Fig. 1 exhibit a clear directional dependence (dichroism) and the similarities in magnitude and line shape of the spectra are apparent. The differences between the four compounds are only due to the appearance of the dipole forbidden M_1 edges ($3s \rightarrow 3d$) of the Ni sample at 112 eV and of the Fe sample at 91 eV. For Ni the M_1 edge lies above the higher-energy branch of the U $O_{4,5}$ edge but for Fe it coincides with the lower-energy branch of the U $O_{4,5}$ edge. These M_1 edges also exhibit a dichroism (43) so that in case of UFe_2Si_2 we mainly rely on the directional dependence of the higher-energy branch of the U $O_{4,5}$ edge at 103 eV. Otherwise, the shape of the U $O_{4,5}$ edges seems fairly robust and independent of the compound under investigations.

In ref. 30 we showed that the multiplet structure of the isotropic NIXS spectrum of URu_2Si_2 is well reproduced with a U^{4+} $5f^2$ ansatz in its J = 4 ground-state multiplet. Higher multiplets do not contribute to the ground state, consistent with the fact that the expected crystal-field splittings as well as the Kondo scale of URu_2Si_2 are much smaller than the spin–orbit splitting of the order of 550 to 600 meV (44, 45). The similarity of the NIXS spectra thus indicates that all of the other compounds with M = Fe, Ni, and Pd show the presence of atomic-like multiplet states and that these are also $5f^2$ based. The presence of hybridization and covalency effects is taken

*The isotropic spectrum $(2 \cdot I_{\vec{q}\|[100]} + I_{\vec{q}\|[001]})/3$ is a pseudoisotropic spectrum in the beyond dipole limit but the deviations are minor; see PhD thesis in Sundermann (42).

into account effectively by the reduction factors of 50% of the Slater integrals $5f$-$5f$ and $5d$-$5f$ (*Materials and Methods*, *Simulation*).

Fig. 2 *A–D* shows the difference spectra (dichroism) of the directional-dependent NIXS data. Given the similarity of the NIXS spectra in Fig. 1 *A–D* it does not come as a surprise that the dichroisms of antiferromagnetic UNi_2Si_2 and UPd_2Si_2 agree as well with the one of URu_2Si_2 in the region of the U $O_{4,5}$ edge. For the Pauli paramagnet UFe_2Si_2, we also find that the dichroism agrees well with that of the other compounds although we have to restrict the comparison to the U signal at 103 eV to avoid the contribution of Fe M_1.

The directional dependence in the spectra is due to the crystal-field splitting of the Hund's rule ground state of the U $5f^2$ configuration. It has a total angular momentum $J = 4$ and is split by the tetragonal (D_{4h} symmetry) crystalline electric field (CEF) into five singlets and two doublets. J remains a good quantum number even in the intermediate coupling regime of uranium so that the CEF wave functions can be written in terms of J_z (Eqs. **1**–**7**):

$$\Gamma_1^{(1)}(\theta) = \cos(\theta)\,|0\rangle + \sin(\theta)\sqrt{\frac{1}{2}}(|+4\rangle + |-4\rangle) \quad [1]$$

$$\Gamma_1^{(2)}(\theta) = \sin(\theta)\,|0\rangle - \cos(\theta)\sqrt{\frac{1}{2}}(|+4\rangle + |-4\rangle) \quad [2]$$

$$\Gamma_2 = \sqrt{\frac{1}{2}}(|+4\rangle - |-4\rangle) \quad [3]$$

$$\Gamma_3 = \sqrt{\frac{1}{2}}(|+2\rangle + |-2\rangle) \quad [4]$$

$$\Gamma_4 = \sqrt{\frac{1}{2}}(|+2\rangle - |-2\rangle) \quad [5]$$

$$\Gamma_5^{(1)}(\phi) = \cos(\phi)\,|\mp 1\rangle + \sin(\phi)\,|\pm 3\rangle \quad [6]$$

$$\Gamma_5^{(2)}(\phi) = \sin(\phi)\,|\mp 1\rangle - \cos(\phi)\,|\pm 3\rangle\,. \quad [7]$$

We now calculate the dichroism of the seven CEF states (Fig. 2 *E–H*) with the full multiplet code Quanty (46) using the same parameters as in ref. 30 (*SI Appendix*). For the mixed singlet states $\Gamma_1^{(1,2)}$ (θ) (Eqs. **1** and **2**) in Fig. 2*E* and the doublet states (Eqs. **6** and **7**) in Fig. 2*G* the extreme dichroisms are given for θ and ϕ equal to 0 and 90°. For other values of θ and ϕ, i.e., in the case of J_z mixtures, the dichroism falls in between the dark and light green (red) lines. In contrast, the dichroisms of the Γ_2, Γ_3, and Γ_4 singlet states in Fig. 2 *F* and *H*, respectively, are given by single lines.

The comparison of the experimental directional dependencies in Fig. 2 *A–D* and the dichroism of the seven crystal-field states in Fig. 2 *E–H* shows immediately that for all four UM_2Si_2 compounds investigated, only the $\Gamma_1^{(1)}$ ($\approx 90°$) and the Γ_2 have the correct sign and magnitude to reproduce the difference spectra.[†] In fact, the experimentally observed magnitude is so large that it excludes any other state and also the $\Gamma_5^{(1,2)}$ that was deduced from O-edge XAS measurements on URu_2Si_2 by Wray et al. (45); for any J_z admixture its directional dependence is either too weak or has the wrong sign (Fig. 2*G*). Note, in spectroscopy, it is always possible to lose dichroism due to, e.g., surface issues in a surface-sensitive technique. NIXS, however, is bulk sensitive and we detect almost the largest possible directional dependence. Finding the same large dichroism in all four compounds, we can safely conclude that it is the singlet

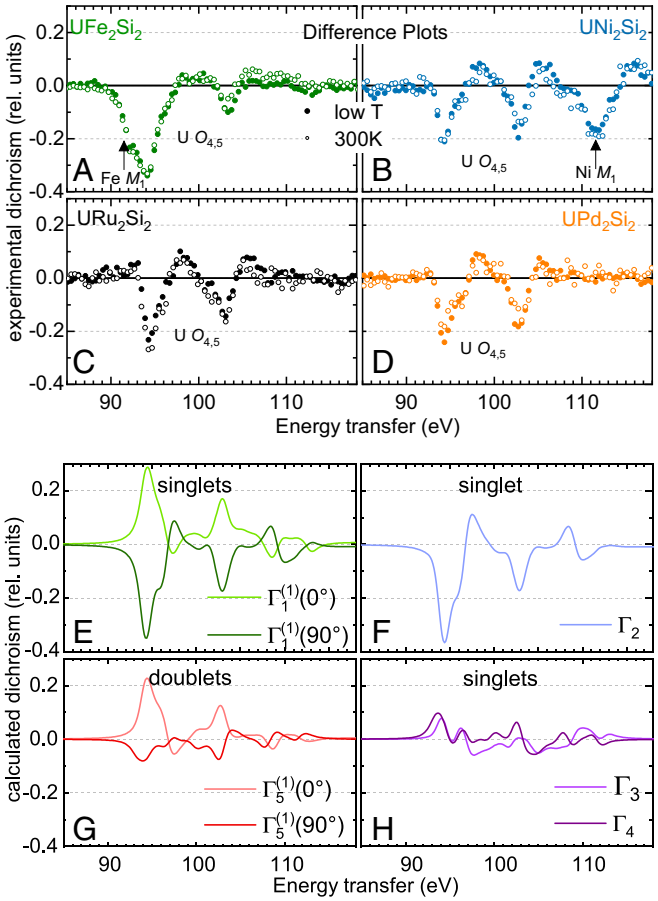

Fig. 2. (*A–D*) Difference plots $I_{\vec{q}\parallel[100]} - I_{\vec{q}\parallel[001]}$ (dichroism) (green for *M* = Fe, blue for Ni, black for Ru, orange for Pd) of UM_2Si_2. Solid circles represent the dichroism at $T < 15$ K and open circles that at $T = 300$ K. The size of the data points represents the statistical error. (*E–H*) Calculated dichroism for the seven crystal-field states. Note the dichroism of $\Gamma_{1,5}^{(1)}$ (0°) is equal to the dichroism of $\Gamma_{1,5}^{(2)}$ (90°) and the one of $\Gamma_{1,5}^{(1)}$ (90°) is equal to the one of $\Gamma_{1,5}^{(2)}$ (0°). In *A* and *C* the extremes are shown for the $\Gamma_1^{1,2}$ (θ) singlet and $\Gamma_5^{(1,2)}$ (ϕ) doublet states with mixed J_z (Eqs. **1**, **2**, **6**, and **7**).

$\Gamma_1^{(1)}$ ($\approx 90°$) or the singlet Γ_2 or, as is explained below, a quasi-doublet made up of the two that determines the local symmetry in the ground state and that the four compounds have this result in common.

Additional data were taken at 300 K to search for the population of CEF excited states. The open circles in Fig. 2 *A–D* represent the directional dependence of the 300-K data. We find that the temperature effect is negligible within the error bars of the experiment for all compounds when comparing the open ($T = 300$ K) with the solid circles ($T < 15$ K). This means that the excited states do not get thermally populated and are quite far away from the $\Gamma_1^{(1)}$ ($\approx 90°$) or the Γ_2 singlet or their quasi-doublet ground state. In ref. 30, we estimated from the lack of temperature dependence that the states with weak dichroism like the $\Gamma_5^{(1)}$ (90°), the Γ_3, and Γ_4 must be higher than 150 K (13 meV), whereas states with stronger opposite anisotropy must be even higher in energy (compare Fig. 2 *E–H*). Only in the case of UPd_2Si_2 the directional dependence seems to have decreased slightly with rising T, hinting toward a smaller CEF splitting with respect to the other compounds.

Relative 5*f* Electron Count with HAXPES. Fig. 3*A* shows the U $4f$ core-level HAXPES data of UFe_2Si_2, URu_2Si_2, UNi_2Si_2, and UPd_2Si_2 at $T = 20$ K after subtracting an integral-type (Shirley)

[†] About 10% ($75° \leq \theta \leq 105°$) of $|0\rangle$ entering the $\Gamma_1^{(1)}$ is possible, giving a slight reduction of the magnitude of the dichroism.

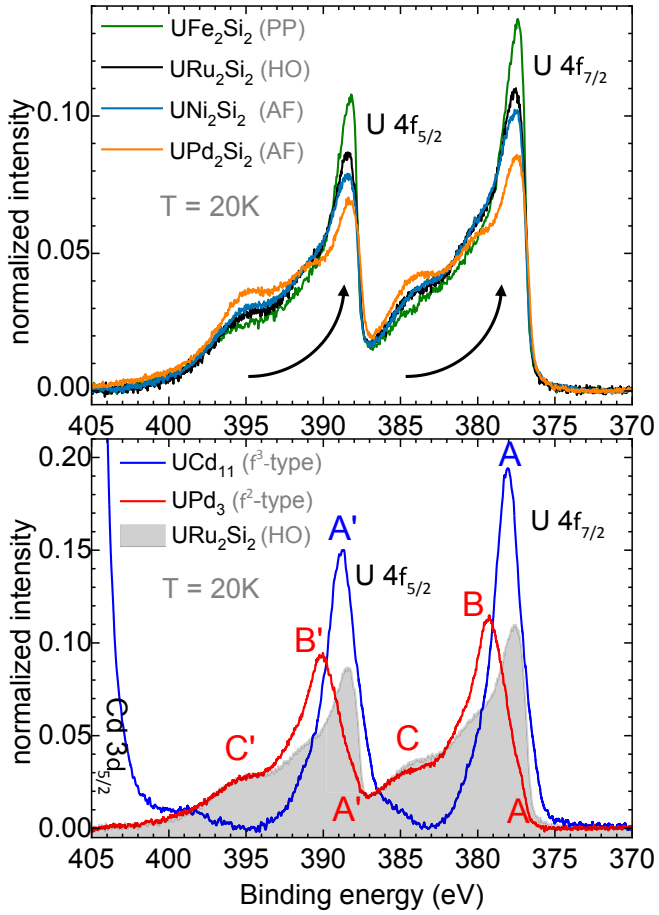

Fig. 3. Background-corrected U 4*f* core-level HAXPES data ($h\nu$ = 5,945 eV) normalized to the integrated intensity (*A*) of UFe_2Si_2 (green), URu_2Si_2 (black), UNi_2Si_2 (blue), and UPd_2Si_2 (orange) and (*B*) of the reference compounds UCd_{11} (blue line) and UPd_3 (red line) with URu_2Si_2 (gray shading) for comparison. Note the expanded y scale in *B*.

background (47) and normalization to the integrated intensity of the U 4*f* core-level emission lines. The U 4*f* core level is spin–orbit split by about 10.8 eV (J = 5/2 and 7/2) and the intensity ratio of the spectral weights assigned to the U $4f_{5/2}$ and U $4f_{7/2}$ turns out to be about 0.8 for all four compounds, which agrees well with the expected value of 6/8 = 0.75. The U 4*f* core-level data consist of the superposition of several U configurations, each with its own multiplet structure. We may crudely describe the spectra with a triple-peak structure at 377.5 (388.3), 380 (390.8), and 384 (394.5) eV for U $4f_{7/2}$ (U $4f_{5/2}$) (Fig. 3*A*).

A systematic change becomes apparent when comparing the 4*f* core-level spectra of the four compounds; from Pd → Ni → Ru → Fe the higher-energy spectral weight at 384 (394.8) eV of the U $4f_{7/2}$ (U $4f_{5/2}$) core level loses spectral weight to the benefit of the peak at 377.5 (388.5) eV. The relative change in spectral weights cannot be due to different crystal structures, different multiplets, or different ground-state symmetries because the four compounds are isostructural and it was shown in the previous section that all four compounds have the same ground-state symmetry arising out of an U^{4+} $5f^2$ configuration. It can therefore only be due to a change in the 5*f*-shell occupation. To be more specific, it must be due to a successive increase of the number of f electrons in the 5*f* shell in accordance with the sequence Pd → Ni → Ru → Fe.

The justification for this interpretation of increasing 5*f* shell filling from M = Pd to Fe is given in Fig. 3*B* which shows the U 4*f* core-level HAXPES data of UCd_{11} (blue line) and UPd_3 (red line). Again the data are normalized to the integrated intensity (note the larger y scale in comparison to Fig. 3*A* to accommodate the strong UCd_{11} signal). UCd_{11} is an example for an intermetallic U compound that has adopted the $5f^3$ configuration (48) and it shows a simple U 4*f* core-level spectrum with peaks at A (U $4f_{7/2}$) and A' (U $4f_{5/2}$). Also the isotropic NIXS spectrum of UCd_{11} is that of a local U f^3, showing the typical shift in energy for a decrease in valence by one (49) and a different lineshape than the f^2 configuration (*SI Appendix*, Fig. S2). UPd_3, on the other hand, is an intermetallic U compound that is quite localized and well described by the U $5f^2$ configuration (50). It shows a pronounced double peak structure B (B') and C (C') for U $4f_{7/2}$ (U $4f_{5/2}$) with some minor, third contribution A (A'), very much in agreement with Fujimori et al. (34).

For a better comparison we overlaid the spectrum of URu_2Si_2 in Fig. 3*B* (see gray shading). This clearly reveals that URu_2Si_2 is intermediate valent because the spectrum contains the A, B, C (A', B', C') structure of the U $5f^2$ and U $5f^3$ features. The peak positions in UPd_3 and UCd_{11} are not precisely the same as in UM_2Si_2 compounds, which can be attributed to the different chemical environment of the U atoms. We further know from a configuration interaction analysis of PES data of, e.g., cerium compounds (51–53) that the higher f-shell filling has an overproportional higher spectral weight, so that, without attempting a quantitative analysis, we can further state that the amount of the $5f^2$ configuration in the initial state must be significant. Another look at Fig. 3*A* lets us then conclude that the U $5f^3$ contribution increases successively from the two antiferromagnets UPd_2Si_2 and UNi_2Si_2 to the hidden-order compound URu_2Si_2 and to the Pauli paramagnet UFe_2Si_2.

Discussion

In NIXS all four compounds exhibit multiplets that are well described with the U $5f^2$ local symmetry; i.e., the multiplets survive even the itineracy in the Pauli paramagnetic state in UFe_2Si_2. Hence, irrespective of the degree of itineracy, the U $5f^2$ configuration determines the local symmetry. This gives credibility to our previous findings of U $5f^2$ multiplets in the hidden-order compound URu_2Si_2 (30). Together with the local symmetry contributions, all four compounds have to be classified as intermediate valent; their ground states are mixtures of the U $5f^2$ and U $5f^3$ configurations. The overall presence of multiplets implies that the dual nature of f electrons not only exists among the antiferromagnetic members, but also persists in the most itinerant members of the UM_2Si_2 family.

Singlets and Quasi-Doublets. The symmetry of the $5f^2$ ground state is, according to our experiment, a singlet state so that the question arises of how this is understood within the context of the antiferromagnetic ground states of UPd_2Si_2 and UNi_2Si_2 with very large ordered moments. After all, only the $\Gamma_5^{(1,2)}$ doublets carry a moment but none of the singlet states do (Table 1). The NIXS data, however, can also be described with two singlets states close in energy, i.e., with a quasi-doublet consisting of the $\Gamma_1^{(1)}$ ($\approx 90°$) and Γ_2 nearby in energy. Here the $\Gamma_1^{(1)}$ has a large $J_z = +4$ and -4 component and the Γ_2 is a pure $J_z = +4$ and -4 state and a quasi-doublet consisting of these two may carry an induced moment. Actually, in the UM_2Si_2 structure, quasi-doublets consisting of $\Gamma_1^{(1,2)}$ and Γ_2 and of Γ_3 and Γ_4 are allowed by symmetry and the intersite exchange of the J_z components leads to the appearance of an ordered magnetic moment. Depending on the energy separation of the quasi-doublet and the admixture of the J_z states in the molecular field ground state composed of either $\Gamma_1^{(1)}$ and Γ_2 or $\Gamma_1^{(2)}$ and Γ_2, any value between 0 and the maximum J_z value may be reached. The range of magnetic moment values is listed in Table 1.

Table 1. Crystal-field states (first column) and their possible ordered magnetic moments (second column), and the possible moments for the quasi-doublets made up from $\Gamma_1^{(1,2)}(\theta)$ and Γ_2, and Γ_3 and Γ_4, respectively (third column)

CEF states	μ_{ord} of singlet states	μ_{ord} of quasi-doublet
$\Gamma_1^{(1,2)}(\theta)$	0	0 to 4 μ_B
Γ_2	0	
Γ_3	0	0 to 2 μ_B
Γ_4	0	
$\Gamma_5^{(1,2)}(\phi)$	μ_{ord} of doublet states 0–3 μ_B	

Our NIXS results reveal that the ground-state symmetry is that of the $\Gamma_1^{(1)}$ or the Γ_2 singlet or the $\Gamma_1^{(1)}$ and Γ_2 quasi-doublet. Such a quasi-doublet can generate induced moments of up to 4 μ_B (Table 1), thus naturally accommodating the large ordered moments that were observed in UPd_2Si_2 (8, 13) and UNi_2Si_2 (11). Even the value of 3.37 μ_B (8) could be explained by such a quasi-doublet. We point out that the idea of using a quasi-doublet to induce magnetic moments and long-range AF magnetic order is not unrealistic. Such an induced magnetic moment scenario has been proposed to explain the magnetic moments in the moderate heavy-fermion compound UPd_2Al_3 with the dual nature of f electrons explaining the heavy bands and dispersive magnetic singlet–singlet excitations mediating the superconducting pairing (37, 38, 54).

Another important aspect of having a quasi-doublet is that it allows for the degeneracy needed for a hidden order to occur in URu_2Si_2. Here, we argue that the orbital degrees of freedom rather than spin form the driving force for the phase transition. Furthermore, it should be mentioned that the Ising-like anisotropy of the static susceptibility is compatible with a quasi-doublet consisting of these two states (55).

Interestingly, local density approximation (LDA) + dynamical mean-field theory calculations found similar states; i.e., the local ground state and the first excited state of the U f^2 configuration in URu_2Si_2 are made up of $\Gamma_1^{(1)}$ and Γ_2 states (ref. 56 and supplementary material of ref. 26). A complex Landau–Ginzburg theory based on these two states (57) was developed for the HO and LAMFM phase of URu_2Si_2, and it accounts for the appearance of moments under applied pressure and other peculiarities of the HO phase. These calculations, however, do not include the full multiplet interactions, i.e., do not take into account the mixture of the orbital momenta $L = 3$, 4, and 5.

***f-d* Hybridization Strength.** We need to look at the hybridization process between the $5f$ and the conduction band electrons to explain the increase of the U^{3+} $5f^3$ spectral weight in the sequence M = Pd(AF) → Ni(AF) → Ru(HO) → Fe(PP).

Fig. 4 *A–D* shows the result of density functional theory (DFT) calculations in the nonmagnetic phase using the full-potential nonorthogonal local orbital code (FPLO) (59) (*SI Appendix*). The partial density of states (DOS) of U $5f$ for J = 5/2 and 7/2; the U $6d$; the transition metal $3d$ or $4d$, respectively; and the Si $3p$ partial DOS are displayed. We observe first of all that there are transition metal d states (colored green [Fe], black [Ru], blue [Ni], and orange [Pd]) present in the energy region where the U $5f_{5/2}$ (colored red) is located, i.e., around the Fermi level. The amount is appreciable for the Fe compound, gets smaller for the Ru and Ni, and is tiny for the Pd. In addition, a closer look reveals that the width of the U $5f_{5/2}$ band is the largest for the Fe compound and the smallest for the Pd, with the Ru and Ni in between. Altogether, this indicates that the mixing

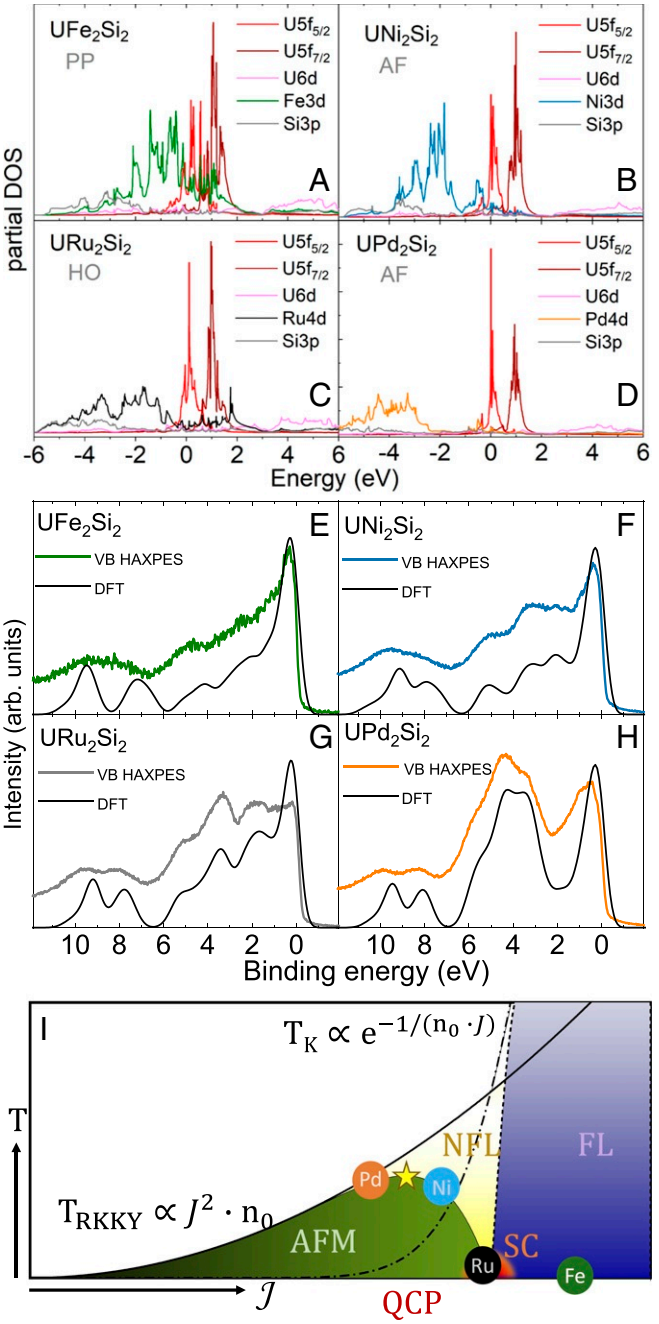

Fig. 4. (*A–D*) Partial DOS of UM_2Si_2 calculated with FPLO (*SI Appendix*). The transition metal partial DOSs of the 3*d* and 4*d* electrons are plotted in green (Fe), blue (Ni), black (Ru), and orange (Pd). (*E–H*) Experimental valence band (VB) HAXPES data of UM_2Si_2 compared to the DFT simulated spectra, which have been obtained from the calculated uranium, transition metal, and silicon partial DOSs weighted for the respective shell-specific photoionization cross-sections. The incident energy was hν = 5,945 eV. (*I*) Doniach-like phase diagram of U $5f^2$ within the quasi-doublet scenario: temperature T versus exchange interaction $\mathcal{J}$ diagram showing the antiferromagnetic regime (AFM, green), the intermediate valent Fermi liquid (FL, purple), the non-Fermi liquid (NFL, yellow), and the superconducting dome (SC, orange) close to the quantum critical point (QCP). The dots represent the location of the respective members of the UM_2Si_2. T_K refers to the Kondo-like temperature and T_{RKKY} to the Ruderman–Kittel–Kasuya–Yosida temperature scale. The yellow star that marks the maximum Néel temperature corresponds to ($\mathcal{J}_{max}$, T_{max}) ≈ (0.27, 0.01) and the critical value is $\mathcal{J}_c$ (QCP) ≈ 0.36 in units of the conduction bandwidth W ∼ 1/n_0, where n_0 is the DOS (58).

or hybridization between the transition metal d and the U $5f$ states is the strongest for Fe, decreases for the Ru and Ni, and is the weakest for the Pd. This trend is fully consistent with the U $4f$ HAXPES result in that the U $5f^3$ contribution decreases successively from the Pauli paramagnet UFe_2Si_2 via the hidden-order compound URu_2Si_2 to the two antiferromagnets UNi_2Si_2 and UPd_2Si_2.

For the interpretation of the calculated partial DOS, one can look at whether the hybridization trend of Fe-Ru-Ni-Pd is reflected by the U-U distances a or the U-transition metal distances $d_{\text{U-TM}}$ across this set of compounds. If so, the f-d hopping integral may play an important role. However, the trend for a, from small to large, is Fe, Ni, Ru, and Pd (*SI Appendix*, Fig. S3). The trend for $d_{\text{U-TM}}$ is, from small to large, Ni, Fe, Ru, and Pd. In other words, already the opposite order of the Ni and Ru compounds in both a and $d_{\text{U-TM}}$ does not favor an interpretation of hopping integral-driven systematics. What is clearly forming a trend in the calculations is the energy position of the d states relative to the U $5f$. In going from M = Fe to Ru to Ni, and to Pd, we observe that the d states are moving to more negative energies and thus farther away from the U $5f$ levels. This strongly suggests that, in terms of a many-body model such as an Anderson impurity or lattice model, it is the $5f$ level position ϵ_f that provides the crucial parameter when comparing this UM_2Si_2 series.

Valence band HAXPES has been used to check whether these DFT predictions are valid. Fig. 4 *E–H* shows the spectra of the four compounds. To compare the DFT results to the experiment, we calculate the valence band spectra by multiplying each of the partial DOSs by their respective shell-specific photoionization cross-section at 5,945 eV photon energy as derived from ref. 60 and by the Fermi function to include only the contributions from the occupied states, followed by a broadening to account for the experimental resolution and intrinsic broadening, and their summation. This was done for all of the partial DOSs included in the calculation (not only the ones shown in Fig. 4 *A–D*). The results are displayed in Fig. 4 *E–H* (black lines). The comparison with valence band HAXPES data confirms the validity of the DFT predictions; the general agreement between experiment and theory is very good. There are deviations in the U $5f$ regions where the calculated intensities are higher than in the experiment since correlation effects were neglected in the DFT, but the lineshape and positions of the silicon, transition metal, and uranium non-f bands are well reproduced. This validates the hybridization picture offered by the DFT calculations and, in turn, provides a consistent reasoning for the increase of the $5f^3$ spectral weight in the sequence M = Pd(AF) → Ni(AF) → Ru(HO) → Fe(PP).

Dual Nature of the 5*f* Electrons. The above findings are very much compatible with the dual-nature idea of f electrons in uranium heavy fermion compounds (35–38). On one hand, we have observed in NIXS the local atomic multiplet structure of the U $5f^2$ configuration in the UM_2Si_2 system. On the other hand, we have noticed from HAXPES the intermediate valent character of U in UM_2Si_2 and that the U $5f^3$ weight increases from Pd to Ni to Ru to Fe. Thus, with increasing f-d hybridization the magnetic moments get suppressed until eventually an intermediate valent Fermi liquid state with enhanced Pauli paramagnetism is reached, thereby showing the impact of the itinerant part. Two of the $5f$ electrons remain localized and form atomic multiplet states whereas a third electron is effectively delocalized with an accordingly renormalized mass.

An important finding is that the four compounds share the same multiplet states for the $5f^2$ configuration, namely the $\Gamma_1^{(1)}$ ($\approx 90°$)/Γ_2 quasi-doublet. This allows us to draw a Doniach-like phase diagram in which the temperature T is plotted versus an effective exchange interaction $\mathcal{J}$, a quantity that is determined by the f-d hopping integral V and the f energy ϵ_f (5) and that can be associated with the degree of delocalization of the third electron. For small $\mathcal{J}$ magnetic order prevails, whereas for large $\mathcal{J}$ a Kondo-like screened (intermediate valent) state forms that is well described in terms of a Fermi liquid (FL) with enhanced Pauli paramagnetism. In the transition region a quantum critical point (QCP) and non-Fermi liquid (NFL) scaling occurs that is often hidden by a superconducting (SC) dome (4, 61). In Fig. 4*I* the Pd member of the family is placed the most to the left because it has the largest ordered moment, followed by the Ni compound that also resides in the AF regime. URu_2Si_2, however, is placed very close to or at the QCP since it is the only compound of the family that exhibits superconductivity and hidden order. UFe_2Si_2, finally, is located on the Kondo-like screened side (PP) to the right of the QCP where the physical properties follow FL scaling.

The application of pressure is known to push URu_2Si_2 into the AF regime (21, 28); i.e., pressure reduces the itinerant part and, in our picture, reduces $\mathcal{J}$. This may seem counterintuitive since pressure will decrease distances and hence increase V so that $\mathcal{J}$ becomes larger since it is proportional to V^2/ϵ_f (5). However, we know pressure will stabilize the f^2 configuration with its smaller ionic radius at the expense of the f^3. This is reflected in this description by the increase of ϵ_f whereby ϵ_f is positive to denote that the f^2 configuration is lower in energy than the f^3. Hence, $\mathcal{J}$ is decreased with pressure because ϵ_f increases more strongly than V^2. With this in mind, we speculate applying pressure to UFe_2Si_2 will also reduce $\mathcal{J}$. And indeed, DFT calculations for a compressed UFe_2Si_2 lattice (62) find that the f^2 configuration is increasingly populated as pressure rises (*SI Appendix*, Fig. S4), thus moving the Fe compound closer to the superconducting–hidden-order regime.

We note that already in 1993, Endstra et al. (12) sorted the members of the UM_2Si_2 family into a Doniach-like phase diagram. The same sequence was suggested, but this was merely based on semiquantitative band structure calculations of the hybridization strength. Which local atomic-like states are active were not known, and moreover, the issue of whether the UM_2Si_2 members have the same multiplet states in common was not even considered. Our experimental findings justify the use of a Doniach-like phase diagram since a common quasi-doublet scenario can be established for the local states together with the observation of strongly varying $5f$ count across the family. Of utmost importance is the fact that the particular quasi-doublet scenario made of J = 4 states allows for the large span of properties across the UM_2Si_2 family, namely to cover antiferromagnetism with very large ordered moments, hidden order, and superconductivity, as well as Pauli paramagnetism.

Conclusion

The dual nature of the $5f$ electrons in four isostructural compounds with very different ground-state properties, namely UPd_2Si_2 (AF), UNi_2Si_2 (AF), URu_2Si_2 (HO), and UFe_2Si_2 (PP), has been shown. The NIXS data of the U $O_{4,5}$ edge reveal multiplets of the localized U $5f^2$ configuration in all four compounds, irrespective of the degree of itineracy, and the directional dependence of NIXS unveils that the different collectively ordered (or nonordered) ground states form out of the same symmetry. The symmetry is determined by the singlet states $\Gamma_1^{(1)}$ ($\approx 90°$) or Γ_2 of the U $5f^2$ Hund's rule ground state, so that only an induced type of order with a quasi-doublet consisting of these two singlet states can explain the large ordered moment of the antiferromagnetic members of the family. The comparison of the $4f$ core-level HAXPES data is meaningful because the four compounds have the same local ground-state symmetry. It reveals the change of the itinerant character within the family. The relative $5f$-shell filling increases successively when going from M = Pd(AF) → Ni(AF) → Ru(HO) → Fe(PP) so that a comprehensive picture is proposed, namely the

sorting of the UM_2Si_2 compounds into a Doniach-like phase diagram.

Materials and Methods

Sample Preparation. The URu_2Si_2 single crystals used for HAXPES were grown by the Czochralski method in a tetra-arc furnace in San Diego, CA from high-purity starting elements (depleted uranium 3N; Ru 3N; Si 6N). Single-crystalline URu_2Si_2 used for the NIXS experiment was grown with the traveling zone method in the two-mirror furnace in Amsterdam, The Netherlands under high-purity (6N) argon atmosphere. Single crystals of UM_2Si_2 with M = Fe, Ni, and Pd were grown in Wroclaw, Poland by the Czochralski pulling technique in ultrapure Ar atmosphere using a tetra-arc furnace. The starting components were high-purity elements (natural uranium 3N; Fe 3N; Ni 4N; Pd 4N; and Si 6N). All single crystals were checked by X-ray Laue diffraction for their single-crystalline nature.

A polycrystalline UPd_3 sample of 1 g was synthesized in Dresden, Germany by arc melting stoichiometric amounts of uranium metal (natural, foil; Goodfellow, 99.98 wt%) with palladium metal (shot; Chempur, 99.99 wt%) under a protective atmosphere of argon gas. The melted button was then placed into an alumina crucible and sealed into a tantalum tube. The sample was heated to 1,400 °C within 6 h, annealed for an additional 6 h, and subsequently furnace cooled to room temperature. The single-phase nature of the sample was deduced from the analysis of powder X-ray diffraction data.

Single crystals of UCd_{11} were grown from Cd flux in Los Alamos. Uranium and cadmium pieces in the molar ratio U:Cd = 1:133 were placed in an alumina crucible and sealed under vacuum in a silica ampoule. The ampoule was heated to 600 °C, held at that temperature for 20 h, and then slowly cooled at 2 °C/h to 400 °C, whereupon the excess Cd flux was removed via a centrifuge.

Experiment. The NIXS measurements were performed at the High-Resolution Dynamics Beamline P01 of the Positron-Elektron-Tandem-Ring-Anlage III (PETRA III) synchrotron in Hamburg, Germany. The end station has a vertical geometry with 12 Si(660) 1-m radius spherically bent crystal analyzers that are arranged in 3×4 matrix and positioned at scattering angles of $2\theta \approx 150^\circ$, 155°, and 160°. The final energy was fixed at 9,690 eV, the incident energy was selected with a Si(311) double monochromator, and the overall energy resolution was ≈0.7 eV. The scattered beam was detected by a position-sensitive custom-made Lambda detector based on a Medipix3 chip. A sketch of the scattering geometry can be found in ref. 63. The averaged momentum transfer was $|\vec{q}| = (9.6 \pm 0.1)$ Å^{-1} at the U $O_{4,5}$ edge. The crystals were mounted in a Dynaflow He flow cryostat with Al-Kapton windows.

The HAXPES experiments were carried out at the beamlines P09 and P22 of the PETRA-III synchrotron in Hamburg, Germany (64, 65). The incident photon energy was set at 5,945 eV. The valence band spectrum of a gold sample was measured to determine the Fermi level E_F and the overall instrumental resolution of 300 meV. The excited photoelectrons were collected using a SPECS225HV electron energy analyzer in the horizontal plane at 90°. The sample emission angle was 45°. Clean sample surfaces were obtained by cleaving the samples in situ in the cleaving chamber prior to inserting them into the main chamber where the pressure was $\sim 10^{-10}$ mbar. The measurements were performed at a temperature of 20 K.

Simulation. The simulations include the spin–orbit as well as Coulomb interactions with atomic values from the Cowan code. The Slater integrals 5*f*-5*f* and 5*d*-5*f* were reduced to account for configuration interaction (66) and covalency effects (67) that are not included in the Hartree–Fock scheme. A reduction of 50% reproduces the energy distribution of the multiplet excitations of the U $O_{4,5}$ edges of the UM_2Si_2. As in ref. 30, the ratio of multipoles was slightly adjusted by using a $|\vec{q}|$ value that is slightly larger than the experimental one. This is necessary because the radial wave functions are based on atomic values. The $J = 4$ multiplet forms the ground state for all finite values of spin–orbit coupling and Coulomb interaction. The relative contributions of the orbital angular momenta $L = 3$, 4, and 5 are 1, 14, and 85% for the present ratio of spin–orbit coupling and Coulomb interaction. A Gaussian broadening of 0.7 eV accounts for the instrumental resolution and a Lorentzian broadening of 1.3 eV for life-time effects. In addition, some asymmetry due to the metallicity of the samples has been described by using a Mahan-type lineshape with an asymmetry factor of 0.18 and an energy continuum of 1,000 eV.

DFT Calculation. Density functional theory-based calculations were performed using FPLO (v.18.00.52), employing LDA and including spin–orbit coupling (fully relativistic calculation). A grid of $15 \times 15 \times 15$ k points and 5,000 energy points (about 1 point every 8 meV) were used for the calculation of the band structure and DOS.

Data Availability. All data are available upon request.

ACKNOWLEDGMENTS. This research was carried out at PETRA III/Deutsches-Elektronen-Synchrotron, a member of the Helmholtz Association of German Research Centers. A.A., A.S., and M. Sundermann gratefully acknowledge the financial support of the Deutsche Forschungsgemeinschaft under Project SE 1441-5-1. A.S. further thanks Quantum Matter and Materials (QM^2) at University of Cologne for financial contribution. M. Szlawska was supported by the National Science Centre of Poland, Grant 2018/31/D/ST3/03295. Research at University of California, San Diego was supported by the US Department of Energy, Office of Basic Energy Sciences, Division of Materials Sciences and Engineering, under Grant DEFG02-04-ER46105 (single-crystal growth) and US National Science Foundation under Grant DMR-1810310 (materials characterization). Work at Los Alamos National Laboratory was also performed under the auspices of the US Department of Energy, Office of Basic Energy Sciences, and Division of Materials Sciences and Engineering. We thank H. Borrman from Max-Planck Institute for Chemical Physics of Solids for his support in handling the U-based samples and J. Grin for support and interest.

1. J. Floquet, "On the heavy fermion road" in *Progress in Low Temperature Physics*, W. P. Halperin, Ed. (Elsevier, 2005), Vol. XV, pp. 139–268.
2. P. Thalmeier, G. Zwicknagl, "Unconventional superconductivity and magnetism in lanthanide and actinide intermetallic compounds" in *Handbook on the Physics and Chemistry of Rare Earths*, J.-C. Bunzli, K. A. Gschneidner Jr, V. Pecharsky, Eds. (Elsevier, 2004), vol. 34, pp. 135–287.
3. P. Coleman, "Heavy fermions: Electrons at the edge of magnetism" in *Handbook of Magnetism. and Advanced Magnetic Materials*, H. Kronmüller, S. Parkin, I. Zutic, Eds. (John Wiley & Sons, 2007), vol. 1, pp. 95–148.
4. H. V. Löhneysen, A. Rosch, M. Vojta, P. Wölfle, Fermi-liquid instabilities at magnetic quantum phase transitions. *Rev. Mod. Phys.* **79**, 1015–1075 (2007).
5. D. I. Khomskii, *Basic Aspects of the Quantum Theory of Solids* (Cambridge University Press, 2010).
6. O. Stockert, S. Kirchner, F. Steglich, Q. Si, Superconductivity in Ce- and U-based "122" heavy-fermion compounds. *J. Phys. Soc. Jpn.* **81**, 011001 (2012).
7. B. White, J. Thompson, M. Maple, Unconventional superconductivity in heavy-fermion compounds. *Physica C* **514**, 246–278 (2015).
8. H. Ptasiewicz-Bak, J. Leciejewicz, A. Zygmunt, Neutron diffraction study of magnetic ordering in UPd_2Si_2, UPd_2Ge_2, URh_2Si_2 and URh_2Ge_2. *J. Phys. F Met. Phys.* **11**, 1225–1235 (1981).
9. K. H. J. Buschow, D. B. de Mooij, Structural and magnetic characteristics of several ternary compounds of the type GdX_2Sb_2 and UX_2Sb_2 (X = 3d, 4d or 5d metal). *Philips J. Res.* **41**, 55–76 (1986).
10. T. T. Palstra, A. A. Menovsky, G. J. Nieuwenhuys, J. A. Mydosh, Magnetic properties of the ternary compounds CeT_2Si_4 and UT_2Si_2. *J. Mgn. Mgn. Mat.* **54–57**, 435–436 (1986).
11. H. Lin, L. Rebelsky, M. F. Collins, J. D. Garrett, W. J. L. Buyers, Magnetic structure of UNi_2Si_2. *Phys. Rev. B* **43**, 13232–13239 (1991).
12. T. Endstra, G. J. Nieuwenhuys, J. A. Mydosh, Hybridization model for the magnetic-ordering behavior of uranium- and cerium-based 1:2:2 intermetallic compounds. *Phys. Rev. B* **48**, 9595–9605 (1993).
13. B. Shemirani *et al.*, Magnetic structure of UPd_2Si_2. *Phys. Rev. B* **47**, 8672–8675 (1993).
14. P. Svoboda, P. Javorsky, F. Honda, V. Sechovky, A. A. Menocsky, Magnetic phases diagrams in UNi_2Si_2. *Centr. Eur. J. Phys.* **2**, 397 (2004).
15. A. Szytuka, L. Gondek, M. Slaski, B. Penc, A. Jezierski, Non-magnetic behaviour of UFe_2Si_2 compound. *J. Alloys Compd.* **44**, 275–278 (2007).
16. T. Plackowski, D. Kaczorowski, J. Sznajd, Magnetic phase diagram and possible Lifshitz critical point in UPd_2Si_2. *Phys. Rev. B* **83**, 174443 (2011).
17. T. T. M. Palstra *et al.*, Superconducting and magnetic transitions in the heavy-fermion system URu_2Si_2. *Phys. Rev. Lett.* **55**, 2727–2730 (1985).
18. W. Schlabitz *et al.*, Superconductivity and magnetic order in a strongly interacting fermi-system: URu_2Si_2. *Z. Phys. B Condens. Matter* **62**, 171–177 (1986).
19. M. B. Maple *et al.*, Partially gapped Fermi surface in the heavy-electron superconductor URu_2Si_2. *Phys. Rev. Lett.* **56**, 185–188 (1986).
20. C. Broholm *et al.*, Magnetic excitations and ordering in the heavy-electron superconductor URu_2Si_2. *Phys. Rev. Lett.* **58**, 1467–1470 (1987).
21. P. G. Niklowitz *et al.*, Parasitic small-moment antiferromagnetism and nonlinear coupling of hidden order and antiferromagnetism in URu_2Si_2 observed by Larmor diffraction. *Phys. Rev. Lett.* **104**, 106406 (2010).
22. P. M. Oppeneer *et al.*, Electronic structure theory of the hidden-order material URu_2Si_2. *Phys. Rev. B* **82**, 205103 (2010).
23. J. A. Mydosh, P. M. Oppeneer, Colloquium: Hidden order, superconductivity, and magnetism: The unsolved case of URu_2Si_2. *Rev. Mod. Phys.* **83**, 1301–1322 (2011).

24. H. Ikeda *et al.*, Emergent rank-5 nematic order in URu_2Si_2. *Nat. Phys.* **8**, 528–533 (2012).
25. J. A. Mydosh, P. M. Oppeneer, Hidden order behaviour in URu_2Si_2 (A critical review of the status of hidden order in 2014). *Philos. Mag.* **94**, 3642–3662 (2014).
26. H. H. Kung *et al.*, Chirality density wave of the "hidden order" phase in URu_2Si_2. *Science* **347**, 1339–1342 (2015).
27. J. A. Mydosh, P. M. Oppeneer, P. S. Riseborough, Hidden order and beyond: An experimental—theoretical overview of the multifaceted behavior of URu_2Si_2. *J. Phys. Condens. Matter* **32**, 143002 (2020).
28. H. Amitsuka *et al.*, Pressure–temperature phase diagram of the heavy-electron superconductor URu_2Si_2. *J. Magn. Magn. Mater.* **310**, 214–220 (2007).
29. W. Knafo *et al.*, Field-induced spin-density wave beyond hidden order in URu_2Si_2. *Nat. Commun.* **7**, 13075 (2016).
30. M. Sundermann *et al.*, Direct bulk-sensitive probe of 5*f* symmetry in URu_2Si_2. *Proc. Natl. Acad. Sci. U.S.A.* **113**, 13989–13994 (2016).
31. A. Santander-Syro *et al.*, Fermi-surface instability at the 'hidden-order' transition of URu_2Si_2. *Nat. Phys.* **5**, 637–641 (2009).
32. J. Q. Meng *et al.*, Imaging the three-dimensional Fermi-surface pairing near the hidden-order transition in URu_2Si_2 using angle-resolved photoemission spectroscopy. *Phys. Rev. Lett.* **111**, 127002 (2013).
33. A. Grassmann, Localization of 5f electrons and correlation effects in the photoemission spectra of UT_2Si_2. *Phys. B Condens. Matter* **163**, 547–549 (1990).
34. S. Fujimori *et al.*, Electronic structure of heavy fermion uranium compounds studied by core-level photoelectron spectroscopy. *J. Phys. Soc. Jpn.* **81**, 014703 (2012).
35. G. Zwicknagl, A. N. Yaresko, P. Fulde, Microscopic description of origin of heavy quasiparticles in upt_3. *Phys. Rev. B* **65**, 081103 (2002).
36. G. Zwicknagl, P. Fulde, The dual nature of 5f electrons and the origin of heavy fermions in U compounds. *J. Phys. Condens. Matter* **15**, S1911–S1916 (2003).
37. P. Thalmeier, Dual model for magnetic excitations and superconductivity in UPd_2Al_3. *Eur. Phys. J. B* **27**, 29–48 (2002).
38. G. Zwicknagl, A. Yaresko, P. Fulde, Fermi surface and heavy masses for UPd2Al_3. *Phys. Rev. B* **68**, 052508 (2003).
39. J. Lee *et al.*, Dual nature of magnetism in a uranium heavy-fermion system. *Phys. Rev. Lett.* **121**, 057201 (2018).
40. R. Caciuffo *et al.*, Uranium $5d-5f$ electric-multipole transitions probed by nonresonant inelastic x-ray scattering. *Phys. Rev. B* **81**, 195104 (2010).
41. M. Sundermann *et al.*, Crystal-field states of UO_2 probed by directional dependence of nonresonant inelastic x-ray scattering. *Phys. Rev. B* **98**, 205108 (2018).
42. M. Sundermann, "f-Electron charge densities probed using core-level non-resonant inelastic x-ray scattering," PhD thesis, University of Cologne (2019).
43. H. Yavas *et al.*, Direct imaging of orbitals in quantum materials. *Nat. Phys.* **15**, 559–562 (2019).
44. S. M. Butorin, Resonant inelastic x-ray scattering as a probe of optical scale excitations in strongly electron-correlated systems: Quasi-localized view. *J. Electron. Spectrosc. Relat. Phenom.* **110–111**, 213–233 (2000).
45. L. A. Wray *et al.*, Spectroscopic determination of the atomic *f*-electron symmetry underlying hidden order in URu_2Si_2. *Phys. Rev. Lett.* **114**, 236401 (2015).
46. M. W. Haverkort, *Quanty* for core level spectroscopy - excitons, resonances and band excitations in time and frequency domain. *J. Phys. Conf. Ser.* **712**, 012001 (2016).
47. S. Hüfner, "The background correction" in *Photoelectron Spectroscopy: Principles and Application* (Springer, ed. 3, 2003), chap. 4.3, pp. 201–205.
48. J. Tobin *et al.*, Separate measurement of the $5f_{5/2}$ and $5f_{7/2}$ unoccupied density of states of UO2. *J. Electron. Spectrosc. Relat. Phenom.* **232**, 100–104 (2019).
49. S. Agrestini *et al.*, Probing the J_{eff}=0 ground state and the Van Vleck paramagnetism of the Ir^{5+} ions in layered $Sr_2Co_{0.5}Ir_{0.5}O_4$. *Phys. Rev. B* **97**, 214436 (2018).
50. K. McEwen *et al.*, Understanding the quadrupolar structures of UPd_3. *J. Magn. Magn. Mater.* **310**, 718–722 (2007).
51. J. C. Fuggle *et al.*, Electronic structure of Ce and its intermetallic compounds. *Phys. Rev. B* **27**, 7330–7341 (1983).
52. O. Gunnarsson, K. Schönhammer, Electron spectroscopies for Ce compounds in the impurity model. *Phys. Rev. B* **28**, 4315–4341 (1983).
53. A. Kotani, T. Jo, J. Parlebas, Many-body effects in core-level spectroscopy of rare-earth compounds. *Adv. Phys.* **37**, 37–85 (1988).
54. N. K. Sato *et al.*, Strong coupling between local moments and superconducting 'heavy' electrons in UPd_2Al_3. *Nature* **410**, 340–343 (2001).
55. G. J. Nieuwenhuys, Crystalline electric field effects in UPt_2Si_2 and URu_2Si_2. *Phys. Rev. B* **35**, 5260–5263 (1987).
56. K. Haule, G. Kotliar, Arrested Kondo effect and hidden order in URu_2Si_2. *Nat. Phys.* **5**, 796–799 (2009).
57. K. Haule, G. Kotliar, Complex Landau-Ginzburg theory of the hidden order in URu_2Si_2. *Europhys. Lett.* **89**, 57006 (2010).
58. T. Schäfer, A. A. Katanin, M. Kitatani, A. Toschi, K. Held, Quantum criticality in the two-dimensional periodic Anderson model. *Phys. Rev. Lett.* **122**, 227201 (2019).
59. K. Koepernik, H. Eschrig, Full-potential nonorthogonal local-orbital minimum-basis band-structure scheme. *Phys. Rev. B* **59**, 1743–1757 (1999).
60. M. B. Trzhaskovskaya, V. K. Nikulin, V. I. Nefedov, V. G. Yarzhemsky, Non-dipole second order parameters of the photoelectron angular distribution for elements Z= 1–100 in the photoelectron energy range 1–10keV. *Atomic Data Nucl. Data Tables* **92**, 245–304 (2006).
61. S. Wirth, F. Steglich, Exploring heavy fermions from macroscopic to microscopic length scales. *Nat. Rev. Mater.* **1**, 16051 (2016).
62. K. Kuwahara *et al.*, High pressure x-ray diffraction study of URu_2Si_2. *Acta Phys. Pol. B* **34**, 4307 (2003).
63. M. Sundermann *et al.*, The quartet ground state in CeB_6: An inelastic x-ray scattering study. *Europhys. Lett.* **117**, 17003 (2017).
64. J. Strempfer *et al.*, Resonant scattering and diffraction beamline P09 at PETRA III. *J. Synchrotron Radiat.* **20**, 541–549 (2013).
65. C. Schlueter *et al.*, "The new dedicated HAXPES beamline P22 at PETRA III" in *AIP Conference Proceedings* (AIP, 2019), vol. 2054, pp. 040010-1–040010-6.
66. A. Tanaka, T. Jo, Resonant 3d, 3p and 3s photoemission in transition metal oxides predicted at 2p threshold. *J. Phys. Soc. Jpn.* **63**, 2788–2807 (1994).
67. S. Agrestini *et al.*, Long-range interactions in the effective low-energy Hamiltonian of Sr_2IrO_4: A core-to-core resonant inelastic x-ray scattering study. *Phys. Rev. B* **95**, 205123 (2017).